Rare Metal Materials and Engineering
Volume 55, Issue 8, August 2026
Available online at www.rmme.ac.cn

Science Press

Cite this article as: Zhu Jialei, Wang Yuke, Zeng Caiyou, et al. Microstructure and Properties of 921A Steel Joints Prepared by Local Dry Underwater Oscillating Laser Welding[J]. Rare Metal Materials and Engineering, 2026, 55(08): 1849-1857. DOI: https://doi.org/10.12442/j.issn.1002-185X.20250473.

ARTICLE

Microstructure and Properties of 921A Steel Joints Prepared by Local Dry Underwater Oscillating Laser Welding

Zhu Jialei, Wang Yuke, Zeng Caiyou, Li Shougen, Zhu Wenlei, Shao Mingxing, Yang Zilong

School of Mechanical Engineering, Beijing Institute of Petrochemical Technology, Beijing 102627, China

Abstract: In response to the need for in-situ repair of deep cracks in a naval ship, a 4 mm-deep 30° U-shaped groove was prepared on 921A steel. Groove filling experiments were conducted using local dry underwater oscillating laser wire feed welding under the conditions of air and shallow water. The microstructure and properties of the welds were analyzed. The results indicate that sound welds without significant defects are obtained in both air and shallow water. Owing to the effective shielding gas protection within the local dry cavity and the rapid cooling effect underwater, the shallow water weld exhibits a bright white surface with densely distributed fish-scale patterns. The air weld includes a higher fraction of acicular ferrite, whereas the rapid cooling in water promotes the formation of lath martensite. The main alloying elements under both environments exhibit a smooth transition near the fusion lines with good metallurgical bonding. However, due to the higher cooling rate in the shallow water compared with that in air, there is a greater fluctuation in elemental distribution, along with higher contents of Si, Mn, and Mo and a slightly lower Cr content in the shallow water weld. The shallow water weld shows higher overall hardness than the air weld, though the hardness distribution trends across different zones are similar in both cases. Tensile tests reveal that fracture occurs in the base metal under both environments, with the tensile strength and yield strength ranking as follows: shallow water weld>air weld>base metal. However, electrochemical corrosion tests indicate that the shallow water weld has inferior corrosion resistance compared to the air weld.

Key words: oscillating laser welding; 921A naval ship steel; local dry underwater welding; microstructure; mechanical properties

1 Introduction

921A naval ship steel is widely used in hull construction due to its excellent strength, toughness, and corrosion resistance[1]. During service, ships are subjected to alternating loads from wave impacts, cargo handling collisions, mooring friction, and other factors, which can lead to the formation of fatigue cracks in critical structural areas such as decks and bulkheads[2]. Under the synergistic influence of the underwater corrosive environment, these cracks may propagate rapidly and develop into deeper flaws, posing a threat to navigation safety. As a result, the in-situ repair of deep cracks has garnered significant research attention.

Groove welding repair has gradually become a common technique for addressing relatively deep cracks, as it can restore structural strength, improve fatigue and corrosion resistance, and extend service life[3–4]. Moreover, local dry underwater laser wire feed welding effectively isolates water and impurities by forming a local dry cavity, thereby reducing defects such as porosity and hydrogen-induced cracking, and significantly enhancing mechanical properties of weld, including strength, toughness, and ductility[5–6]. Zhang et al[7] investigated the influence of gas pressure on laser-welded 316L stainless steel joints using a self-developed double-layer air chamber local dry system, achieving high-quality welds, though some porosity remained. Fu et al[8] performed

Received date: September 16, 2025
Foundation item: Program of Beijing Municipal Education Commission (KM202310017006); Key Supported Project of the Joint Fund of the National Natural Science Foundation of China (U22B20127); Key R&D Program Project of Hebei Province: Development and Application of Robot Laser-Arc Hybrid Welding Technology (23311802D); High-Level Scientific Research and Innovation Team Construction Support Program Project of Beijing Municipal Colleges and Universities (BPHR20220110)
Corresponding author: Li Shougen, Ph. D., School of Mechanical Engineering, Beijing Institute of Petrochemical Technology, Beijing 102627, P. R. China, E-mail: lishougen@bipt.edu.cn

underwater laser wire feed welding on 304 stainless steel with a custom double-sided gas protection device, producing defect-free joints. Their results also indicated that the higher cooling rates can refine grain size but increase the content of lamellar ferrite in the fusion zone, reducing joint toughness. To further mitigate porosity and improve metallurgical quality and mechanical properties, researchers have begun incorporating laser oscillation into the welding process. This technique expands the thermal influence zone, improves gap-filling capability, enhances molten pool stability, and promotes grain refinement through agitation, thereby reducing defects such as cracks and porosity[9–13]. Yang et al[14] employed a Ni interlayer in laser oscillating welding of 2205 duplex stainless steel and found that the beam oscillation promotes uniform Ni distribution and microstructural homogeneity. Shahin et al[15] demonstrated the improved joint quality in Fe-Al laser oscillating welding, with more equiaxed grains and reduced hot cracking susceptibility. Li et al[16] reported that an oscillation amplitude of 2.0 mm and a frequency of 150 Hz result in wider and shallower welds, reducing the risk of lack of sidewall fusion and finger-like penetration. Wang et al[17] studied the effect of laser oscillation patterns on 5754 aluminum alloy welded joints and showed that the ∞-shaped oscillation mode can effectively minimize porosity and improve the weld quality. Nevertheless, few studies have addressed the application of local dry underwater laser oscillating welding in ship repair.

To address this gap and enable in-situ underwater repair of deep cracks on hull surfaces, this study combines the benefits of local dry underwater laser welding and laser oscillating welding. Using a self-developed drainage device and welding test system, the local dry underwater laser oscillating welding experiments are conducted in both air and shallow water (water depth of 200 mm) to analyze the microstructural characteristics of 921A steel welds. The research aims to clarify the influence of shallow water on the microstructure and properties of the welded joints, providing a theoretical basis for the emergency in-situ repair of naval vessels and offshore platforms.

2 Experiment

The experimental materials consisted of 921A steel and WM960S welding wire with a diameter of 1.2 mm, whose chemical composition is provided in Table 1. The test specimens were machined into plates measuring 600 mm in length, 150 mm in width, and 10 mm in thickness. Argon was employed as the shielding gas.

To meet the experimental requirements for shallow-water welding repair of 921A steel, a self-developed local dry underwater oscillating laser welding system was established, as illustrated in Fig.1. The system primarily consists of a laser unit, water chiller, robotic arm, water drainage device, wire feeder, oscillating laser welding head, testing water tank, and ancillary components. During welding in both air and shallow water, argon gas was supplied at a rate of 30 L/min in the coaxial direction to protect the weld. In the shallow water, argon was continuously fed into the telescopic adaptive water drainage device at the same rate to ensure the formation of a local dry cavity during welding repair.

In comparison with V-shaped grooves, U-shaped grooves can enhance molten pool stability during welding. Furthermore, an angle of 15° between the side tangent and the symmetry axis effectively prevents defects such as lack of fusion at the groove root[18]. Therefore, the groove used in this study is a 4 mm deep U-shaped groove with a 15° angle between the side tangent and the symmetry line. Through experiments, four passes of filling welding were performed on the groove, and the groove shape and simulated weld beads are shown in Fig. 2. Based on preliminary single-factor and orthogonal experiments, the optimization of welding process parameters under different environments was conducted, with weld

Table 1 Chemical composition of 921A steel and WM960S welding wire (wt%)

Material	C	Si	Cr	Mn	Ni	Mo
921A steel	0.040	0.290	1.140	0.390	2.730	0.250
WM960S welding wire	0.041	0.495	-	1.380	2.800	0.268

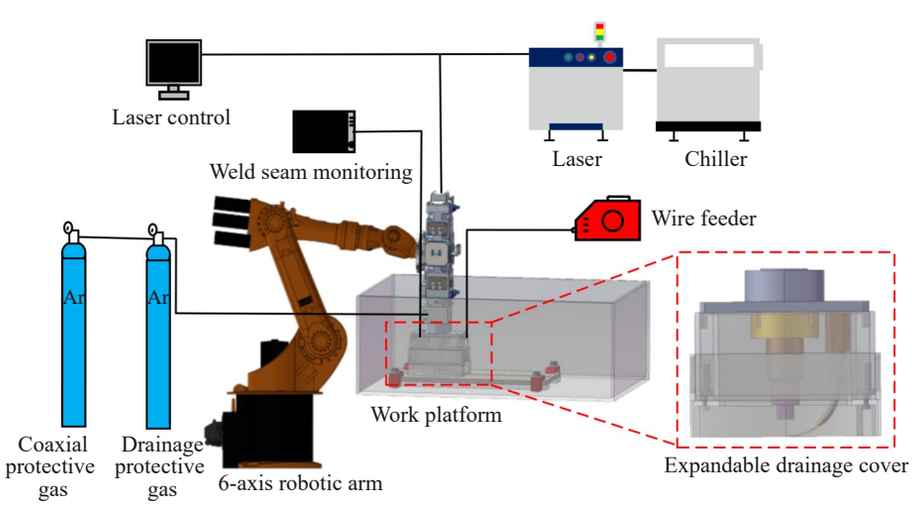

Fig.1 Schematic diagram of repair system of local dry underwater oscillating laser welding

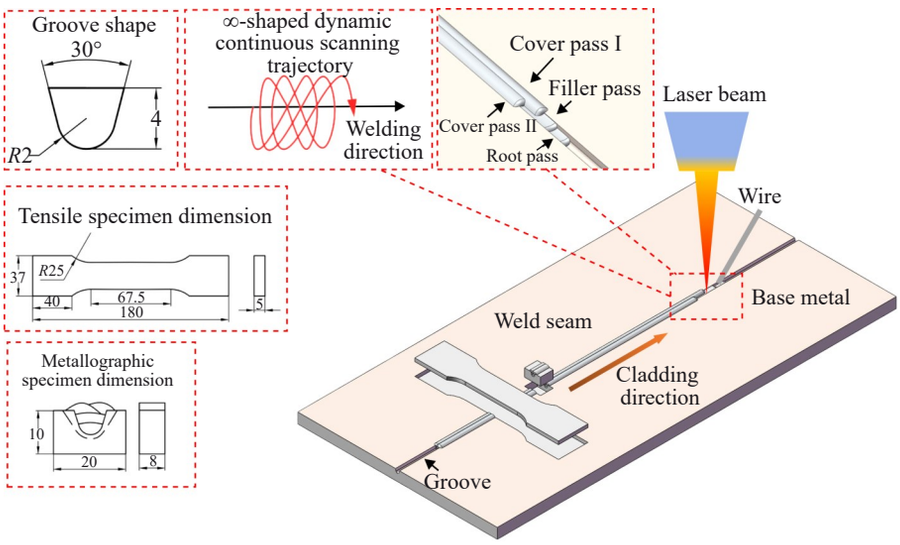

Fig.2 Schematic diagrams of simulated weld bead, groove shape, sampling positions, and dimensions of tensile and metallographic specimen

geometric dimensions as the optimization targets. Ultimately, the same welding parameters were adopted for both air and shallow water environments, including a laser power of 5000 W, a welding speed of 7 mm/s, a wire feeding speed of 280 cm/min, laser oscillation in the ∞-shaped pattern with an oscillation frequency of 200 Hz and an oscillation amplitude of 5 mm.

Following welding, comprehensive microstructural characterization and property evaluation of the welds were performed. Specimens for metallographic examination, hardness testing, tensile testing, and electrochemical analysis were prepared along the direction perpendicular to the weld using wire electrical discharge machining. The sampling method and specimen dimensions are shown in Fig. 2, where the metallographic, hardness, and electrochemical specimens have the same dimensions. The specimens were subsequently ground with progressively finer sandpapers (up to 2000# grit to control surface roughness), followed by polishing and etching using a standard metallographic etchant to reveal the microstructure. Microstructural observation of the welded joints was conducted using a Leica DMi8c optical microscope. Phase composition analysis within the weld was conducted via X-ray diffractometer (XRD, FOCUS diffractometer), employing a scanning range of 25° to 100°. Elemental composition across micro-regions of the specimens was analyzed by energy-dispersive X-ray spectroscope (EDS) on a Quanta 400 field-emission scanning electron microscope (FE-SEM), with point scanning adopted to determine elemental distribution within the weld zone. Hardness measurements were taken using an HVS-1000Z Vickers hardness tester under a 500 g load and a dwell time of 10 s. Tensile tests were performed with an MTS C64.305 tensile testing machine. For electrochemical testing, the back of each specimen was connected to a copper wire using conductive copper tape, and the specimens were then mounted in epoxy resin. Electrochemical impedance spectroscopy (EIS) and potentiodynamic polarization curves of the welded joints from both environments were tested in a 3.5% NaCl solution using a VersaSTAT 3F electrochemical workstation.

3 Results and Discussion

3.1 Macrostructure

Fig. 3a and Fig. 3b present the surface morphologies of the welds prepared in air and shallow water, respectively. Both welds exhibit a continuous and uniform appearance without significant defects. Due to the combined effects of the stable local dry argon cavity formed by the water drainage device and the rapid cooling inherent to the shallow water environment, the weld prepared underwater demonstrates a lower degree of oxidation compared to that prepared in air. Moreover, the shallow water weld exhibits a characteristic dense, bright-white fish-scale pattern on its surface. Fig. 3c and Fig. 3d present the macroscopic cross-sectional morphologies of the welds prepared in air and shallow water, respectively. The weld metal is well bonded to the base metal (BM), each weld layer shows a smooth and arc-shaped transition, and the overall weld exhibits a characteristic W-shaped profile. No significant defects, such as pores, cracks, inclusions, or lack of fusion, are observed.

To investigate the influence of the environment on the weld formation of 921A steel during oscillating laser welding, a systematic comparison of the weld reinforcement, weld width, and weld penetration in air and shallow water was conducted, with the results as shown in Fig. 4. Fig. 4a presents the overall weld reinforcement curves: the weld reinforcement in the shallow water drops sharply after reaching a peak value of 1.2 mm, featuring a relatively high overall peak and significant fluctuations; in contrast, the weld reinforcement in the air is generally lower with a peak value of 0.79 mm and distributes more smoothly along the weld width direction. Fig. 4b and Fig. 4c further reveal the differences in weld geometric characteristics between the two environments. Both the overall weld and each layered weld bead in air exhibit

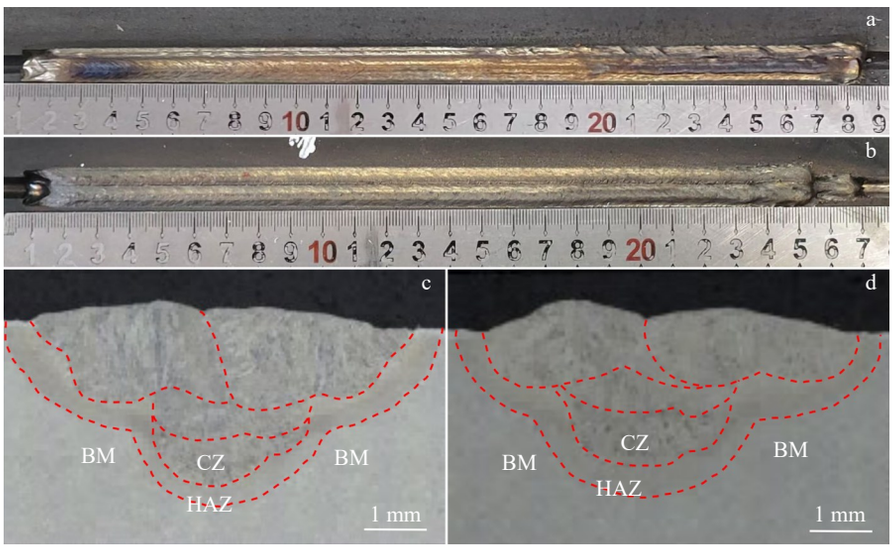

Fig.3 Appearances (a–b) and cross-sectional morphologies (c–d) of the welds prepared in air (a, c) and shallow water (b, d) (HAZ represents the heat-affected zone, and CZ denotes the cladding zone)

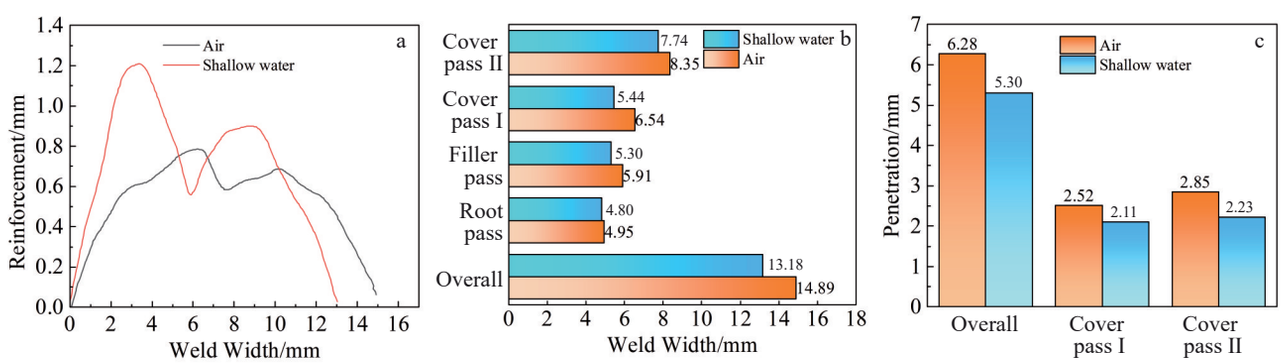

Fig.4 Weld reinforcement (a), weld width (b), and weld penetration (c) of two weld beads prepared in air and shallow water

larger weld width and penetration than those in the shallow water. The above phenomena indicate that the shallow water environment exerts a significant inhibitory effect on the heat input and molten pool development during the welding process, which mainly stems from the impact of the environmental medium on the weld molten pool behavior. In the shallow water, the strong cooling effect of water leads to a sharp increase in cooling rate of the welding zone and the decrease in molten pool fluidity, preventing the sufficient spreading of weld metal and thus resulting in relatively high and significantly fluctuating weld reinforcement. Meanwhile, the rapid cooling of the welding zone by the water medium also significantly weakens the effective heat input, which not only inhibits the further melting of BM but also restricts the conduction of laser energy to the depth of the material, ultimately leading to a decrease in weld width and penetration. The above analysis indicates that the influence of cooling conditions on weld bead formation is consistent across layers. Specifically, whether for single-layer single-pass or multi-layer multi-pass welds, their morphological evolution is controlled by the difference in cooling rate dominated by the welding environment, and the formation mechanism of each single-layer weld bead can effectively reflect the formation characteristics of the overall weld bead.

3.2 Microstructure

To further investigate the influence of air and shallow water environments on the microstructural characteristics of the welded joints, metallographic analysis was conducted on the bottom CZ, middle CZ, and surface CZ of the welds, as shown in Fig.5 and Fig.6.

As shown in Fig.5b and Fig.6b, the microstructure in the air consists of relatively coarse grains with a higher content of acicular ferrite (AF). In contrast, the microstructure in the shallow water is predominantly composed of lower bainite (LB) and lath martensite (LM). This difference can be attributed to the rapid cooling rate in the shallow water, which inhibits austenite-to-ferrite transformation even within the ferrite transformation temperature range[19]. As a result, the root bead in the shallow water primarily contains LB and LM.

As shown in Fig.5c and Fig.6c, the grain size in the filling zone is larger than that in the root bead, accompanied by an increased amount of AF. This is attributed to the higher heat input in the filling zone induced by preheating from the root

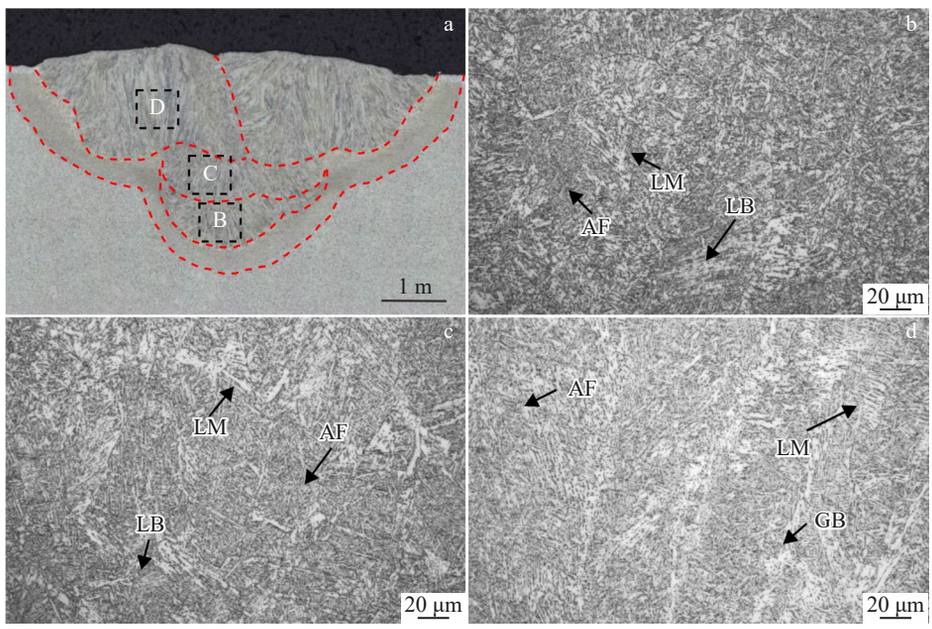

Fig.5 Schematic diagram of metallographic sampling points (a) and microstructures (b–c) of weld bead prepared in air: (b) root pass of region B marked in Fig.5a; (c) filler pass of region C marked in Fig.5a; (d) cover pass of region D marked in Fig.5a

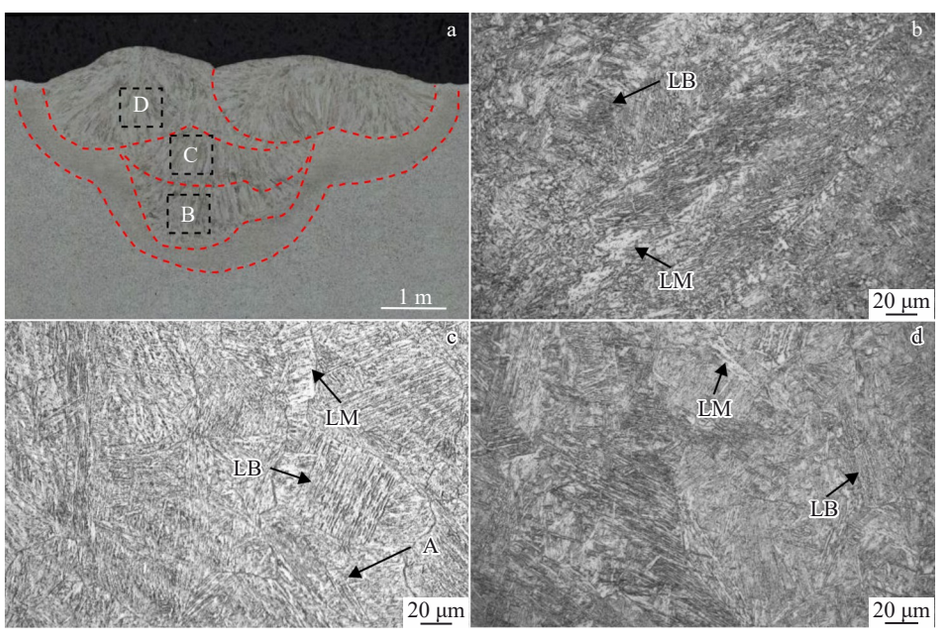

Fig.6 Schematic diagram of metallographic sampling points (a) and microstructures (b–c) of weld bead prepared in the shallow water: (b) root pass of region B marked in Fig.6a; (c) filler pass of region C marked in Fig.6a; (d) cover pass of region D marked in Fig.6a

layer and reheating from the capping layer. Furthermore, the ∞-shaped laser oscillation reduces the temperature gradient within the molten pool[20–21], leading to a slower cooling rate and promoting grain coarsening. These conditions facilitate the transformation of austenite (A) to ferrite, resulting in a higher AF content. Compared to that in air, the microstructure in the shallow water exhibits more LB and less AF, owing to its faster cooling rate, which favors the formation of LB over AF.

As shown in Fig. 5d and Fig. 6d, the capping zone exhibits finer grains, a higher fraction of LM, and less AF compared to the filling zone. Unlike the filling zone, the capping zone does not undergo reheating, resulting in a higher cooling rate that suppresses AF formation and enhances martensitic transformation. In this region, the microstructure in the air contains more AF, while that in the shallow water is characterized by a greater amount of LM due to the accelerated cooling rate, which promotes martensite formation and restricts ferrite growth.

3.3 EDS analysis

To investigate the effects of welding environments on the elemental distribution characteristics and interfacial

metallurgical bonding behavior of oscillating laser welded joints of 921A steel, EDS line scanning analysis was conducted on the welds prepared in air and shallow water, with sampling positions at the fusion lines of each layer of weld beads in the weld center region. The results are presented in Fig. 7. Among them, Fig. 7a – 7c illustrate the elemental distribution of three regions in air, namely cover pass to filler pass, filler pass to root pass, and root pass to BM, while Fig. 7d–7f show the elemental distributions of the same regions in the shallow water. The dashed lines in Fig. 7 indicate the positions of the weld fusion lines.

The analysis results indicate that in both air and shallow water, the major alloying elements all exhibit a certain degree of gradual decrease near the fusion lines, but the overall transition is smooth, without an obvious abrupt interface of element content. This result demonstrates that during the oscillating laser welding process, the intense stirring effect of the laser on the molten pool and the high-temperature thermal cycle promote sufficient melting and interdiffusion of the materials on both sides of the interface, thereby achieving good metallurgical bonding.

Further comparison of the elemental distribution curves under the two environments reveals that the fluctuation amplitude of each element signal of shallow water weld is significantly larger than that of air weld. This compositional inhomogeneity at the microscale is mainly attributed to the high cooling rate induced by the local dry shallow water environment. The intense quenching effect of water significantly shortens the residence time of the molten pool and accelerates the solidification process, leading to the solidification of alloying elements before the completion of diffusion homogenization, thus forming local enrichment or depletion regions.

Table 2 presents the chemical element contents of the welds prepared in air and shallow water. The data show that compared with those of air weld, the contents of Si, Mn, and Mo of shallow water weld are higher, while the Cr content is slightly lower. This difference is closely related to the diffusion behaviors of different elements and cooling conditions. During welding in shallow water, the higher cooling rate inhibits the further diffusion of elements such as Si, Mn, and Mo from the molten pool to BM, resulting in more of these elements being retained in the weld center region. In contrast, the Cr content in the welding wire is extremely low, so the Cr in the weld is mainly derived from the dilution and diffusion of the BM. Although Cr has the characteristics of a high melting point and a low diffusion coefficient, the stirring effect of laser oscillation on the molten pool can still promote its migration from the BM to the weld. However, the short residence time of the molten pool in shallow water welding restricts the sufficient diffusion of Cr, leading to a slightly lower Cr content in the weld prepared in shallow water than that in air.

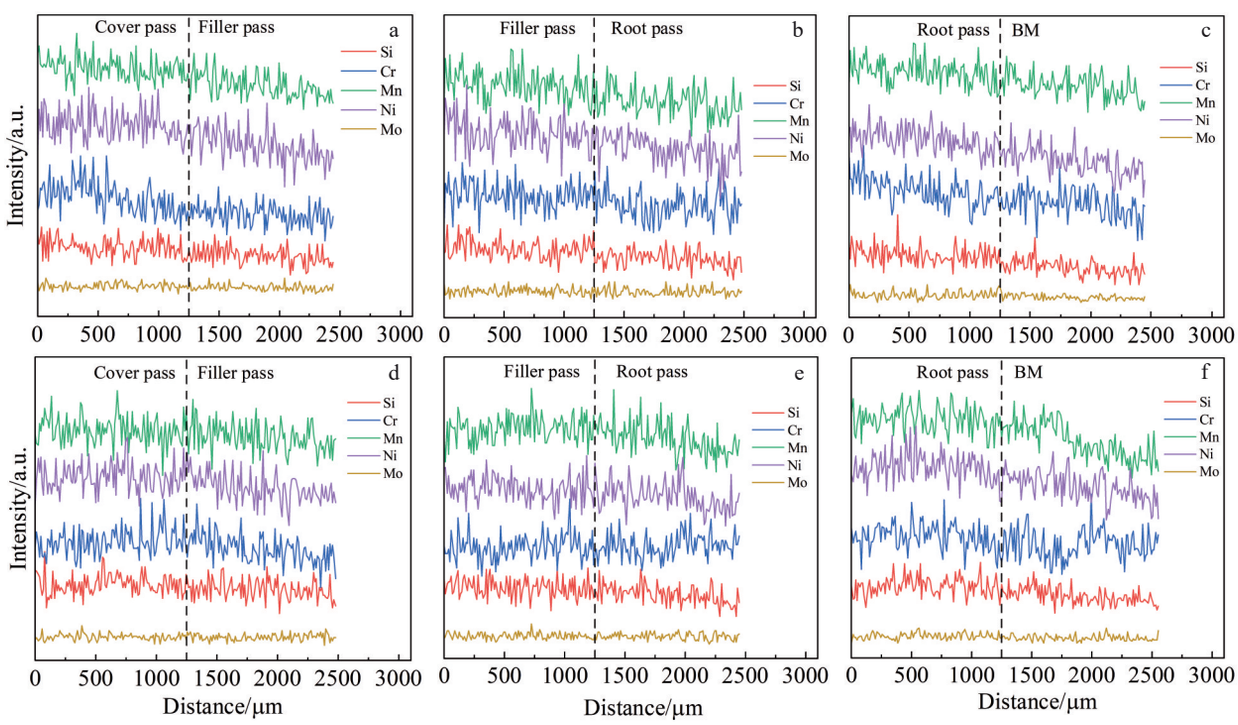

Fig.7 EDS line scanning results of the specimens welded in different environments: (a–c) air; (d–f) shallow water

Table 2 EDS results of welds prepared in air and shallow water (wt%)

Environment	Si	Cr	Mn	Fe	Ni	Mo
Air	0.27	0.62	0.63	89.50	2.23	0.16
Shallow water	0.53	0.47	0.92	88.75	2.21	0.30

3.4 Mechanical property

3.4.1 Hardness

Vickers hardness measurements were conducted across different regions of the welds, with measurements taken at

intervals of 0.5 mm. A schematic diagram of the hardness test locations is provided in Fig.8a.

Fig. 8b and Fig. 8c present the hardness distributions of the welds prepared in air and shallow water. The higher cooling rate in the shallow water promotes the formation of martensite and bainite, resulting in an overall increase in weld hardness compared to that in the air.

Under both conditions, the hardness in the capping and filling zones exhibits a double-peak distribution, descending in the order: HAZ>CZ>BM. This distribution is attributed to the overheating in HAZ during welding, which forms coarse grains consisting mainly of LM, thereby forming a hardness peak. In CZ, the ∞-shaped oscillating welding promotes more uniform heat distribution, avoiding localized rapid cooling[22], and leading to a relatively even hardness profile. This region, composed primarily of ferrite with minor amounts of martensite and bainite, exhibits higher hardness than BM, which has a sorbitic structure. In the root zone, the hardness follows the order: CZ>HAZ>BM. Due to direct contact with the low-temperature BM, the root zone experiences rapid cooling and significant grain refinement, resulting in the highest hardness among all regions.

Across the various weld zones, the hardness decreases in the sequence: root zone>capping zone>filling zone. The root zone benefits from high cooling rates and low heat input, yielding fine grains and high hardness. In contrast, the filling zone undergoes multiple thermal cycles during welding, leading to a high content of AF and associated structural softening, resulting in a decrease in hardness. Within the HAZ, the hardness follows the order: capping zone>filling zone>root zone. The capping and filling zones receive higher heat input, allowing more complete homogenization of austenite. After cooling, these regions form harder martensitic structures. However, subsequent preheating and tempering in the filling zone cause partial tempering of the martensite, reducing its hardness relative to the capping zone. The root zone in HAZ experiences the shortest thermal exposure, resulting in insufficient microstructural transformation and the lowest hardness among the three zones.

3.4.2 Tensile properties

The tensile properties of welded joints prepared in air and shallow water are summarized in Fig. 9. Tensile specimens under both conditions fractured within BM region, indicating that both the strength and ductility of the weld zones exceed those of BM. This behavior can be attributed to rapid solidification and dynamic recrystallization in CZ, which result in significantly refined and homogeneously distributed grains. The enhanced mechanical properties are attributed to grain refinement strengthening.

The tensile curves indicate that the tensile strength and yield strength of the welds prepared in air are 838 MPa and 742 MPa, respectively; while those in the shallow water are 857 MPa and 759 MPa, respectively. The tensile strength and yield strength of the weld prepared in the shallow water are higher than those prepared in air. This improvement can be mainly ascribed to the higher cooling rate underwater, which promotes the formation of a martensite/bainite duplex structure with elevated dislocation density. According to EDS results, the higher Mo content of the shallow water weld further promotes the nucleation and growth of bainite with an interlaced morphology[23], thereby contributing to the increase in strength.

3.5 Corrosion resistance

Fig.10a presents the potentiodynamic polarization curves of the welds prepared in air and shallow water. The specific values of corrosion current density (I_{corr}) and corrosion potential (E_{corr}) of the welds are as follows: 3.28×10^{-5} A/cm^2 and -0.694 V in air, and 6.37×10^{-5} A/cm^2 and -0.781 V in shallow water, respectively. The higher I_{corr} and more negative E_{corr} of the weld prepared in shallow water indicate inferior corrosion resistance compared to those prepared in air.

As shown in the Nyquist plots and equivalent circuit models in Fig. 10b, the capacitive arc radius of the weld prepared in shallow water is significantly smaller than that prepared in the air, further confirming its reduced corrosion resistance. EIS fitting parameters are summarized in Table 3. The surface film resistance (R_{film}) of weld prepared in air is notably higher than that prepared in shallow water, suggesting the formation of a denser and more protective oxide layer. This finding is further corroborated by EDS results: the weld prepared in shallow water has a lower Cr content, resulting in insufficient element Cr during the nucleation and growth of the passive film, which restricts the complete formation of a highly stable Cr_2O_3 passive film[24]. Meanwhile, the lower dispersion index (n_{film}) of the shallow water weld implies the greater deviation from ideal capacitive behavior. This is

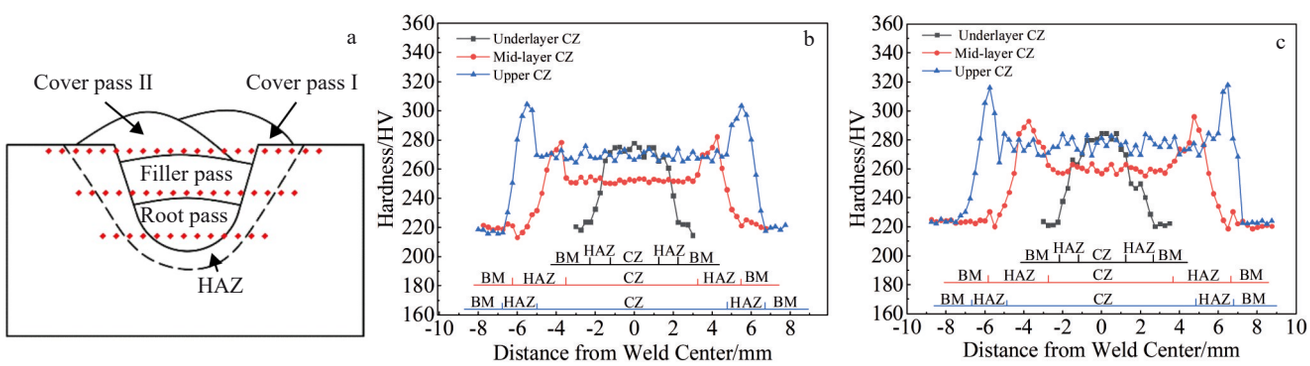

Fig.8 Schematic diagram of hardness measurement points (a) and hardness distributions of the welds prepared in air (b) and shallow water (c)

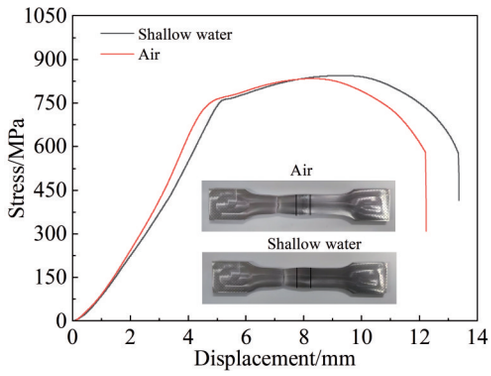

Fig.9 Tensile curves of welds in two environments

attributed to the structural defects or inhomogeneities within the surface film, which lead to uneven current distribution. In addition, the larger polarization resistance (R_p) of the weld prepared in air corroborates its enhanced corrosion resistance, which is consistent with the polarization curve.

Fig.10c and Fig.10d display the Bode impedance and phase angle plots, respectively. At equivalent frequencies, the shallow water weld exhibits lower impedance modulus, confirming its lower corrosion resistance. The maximum phase angle is approximately 60°–65° and 55°–60° for the weld prepared in the air and the shallow water, respectively. The decrease in the maximum phase angle further reflects an accelerated corrosion rate of the shallow water weld.

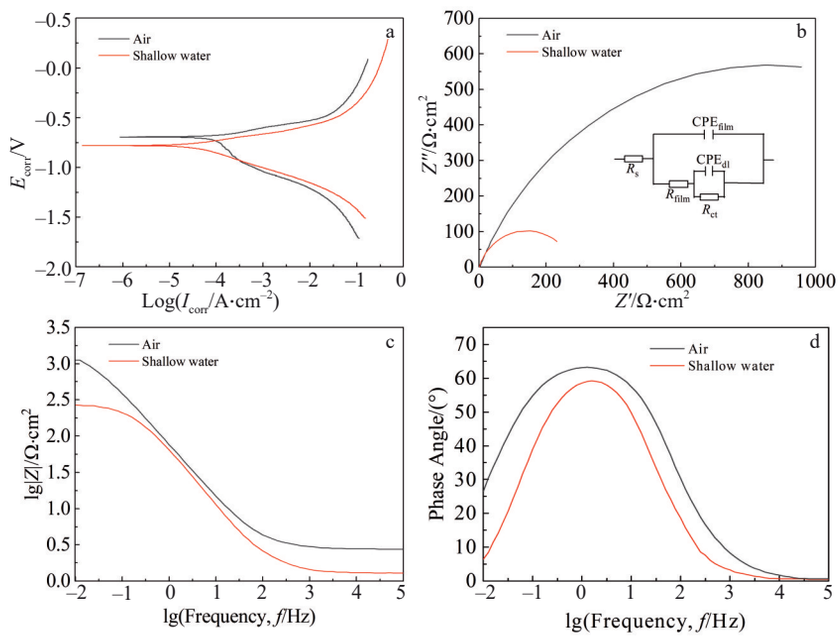

Fig.10 Potentiodynamic polarization curve (a), Nyquist plot (b), Bode-impedance plot (c), and Bode-phase plot (d) of different welds

Table 3 EIS fitting results of welds prepared in different environments

Environment	Solution resistance, R_s/Ω·cm^2	CPE$_{film}$		Film resistance, R_{film}/Ω·cm^2	CPE$_{dl}$/ Ω^{-1}·cm^{-2}·S^n	Charge transfer resistance, R_{ct}/Ω·cm^2	Polarization resistance, R_p/Ω·cm^2
		Y_{film}/ Ω^{-1}·cm^{-2}·S^n	Dispersion index, n_{film}				
Air	2.7450	3.221×10^{-3}	0.782	15.87	7.575×10^{-5}	1709.0	1724.870
Shallow water	1.2889	7.609×10^{-3}	0.739	8.403	6.277×10^{-4}	275.4	283.803

Note: the double-layer constant phase element (CPE$_{dl}$) in the equivalent circuit is employed to describe the non-ideal capacitive behavior at the electrode/solution interface.

4 Conclusions

1) Sound and continuous welds without defects are achieved in both air and shallow water. Compared with the weld prepared in air, the weld prepared in shallow water shows less surface oxidation, yet it has higher reinforcement and smaller weld width and penetration.

2) Cooling rate and the remelting effect induced by laser oscillation are the primary factors influencing microstructural evolution and elemental distribution. In the air, the root zone cools slowly, resulting in a high content of AF. In contrast, the rapid cooling in shallow water promotes the formation of LB and LM. The filling zone experiences multiple thermal cycles, reducing the cooling rate and leading to coarser AF grains. The capping zone, unaffected by subsequent thermal cycles, shows decreased AF content and increased LM content. Furthermore, in both environments, the major alloying elements exhibit a smooth transition near the fusion lines with excellent metallurgical bonding. While the higher cooling rate in the shallow water results in greater fluctuation in elemental distribution, along with higher contents of Si, Mn, and Mo and a slightly lower Cr in the welds.

3) Owing to microstructural strengthening, the overall hardness of the weld prepared in shallow water is higher than that prepared in the air. Both welds exhibit similar hardness distribution characteristics: the filling and capping zones show a double-peak profile, ordered as HAZ>CZ>BM, while the root zone follows the order of CZ>HAZ>BM. Across the entire weld, the hardness decreases in the order of root zone>capping zone>filling zone; and within the HAZ, the hardness decreases in the order of capping zone>filling zone> root zone. Tensile tests indicate that the fracture occurs in BM of both welds, confirming the superior tensile properties of the weld zone. The tensile strength of the weld prepared in shallow water reaches 857 MPa, which is higher than the 838 MPa observed in the weld prepared in air.

4) Electrochemical corrosion analysis of the welds reveals that the weld prepared in shallow water exhibits lower values in E_{corr}, capacitive arc radius in the Nyquist plot, R_p, impedance at identical frequencies, and maximum phase angle compared with the weld prepared in air, indicating inferior corrosion resistance.

References

1 Zhou Feihong, Zhu Jialei, Kou Rongkui *et al. Applied Laser*[J], 2023, 43(10): 22 (in Chinese)

2 Xu Zhihua. *Shipping Materials & Market*[J], 2024, 32(4): 99 (in Chinese)

3 Zheng Bofang. *Research on Welding Technology of Narrow Gap Groove Welding in Misaligned Laser CMT Hybrid Welding*[D], Tianjin: Tianjin University, 2022 (in Chinese)

4 Xu Zilong. *Study on Welding Manufacturing Process and Joint Properties of 16MnDR Nuclear Vessel*[D], Lanzhou: Lanzhou University of Technology, 2021 (in Chinese)

5 Danbi S, Jungsoo C, Dongsig S *et al*. *Metals*[J], 2022, 12(11): 1904

6 You Jiayu, Hu Chenyu, Li Yongqing *et al*. *Rare Metal Materials and Engineering*[J], 2024, 53(8): 2314 (in Chinese)

7 Zhang Hengquan, Zhou Xiaohui, Wei Lianfeng *et al*. *Chinese Journal of Lasers*[J], 2023, 50(12): 58 (in Chinese)

8 Fu Y L, Guo N, Cheng Q *et al*. *Journal of Materials Research and Technology*[J], 2020, 9(6): 15648

9 Yu K, Tan Z J, Zeng C Y *et al. Optics & Laser Technology*[J], 2025, 192: 113947

10 Li Tian. *Mechanism Study of the Effect of Interfacial Intermetallic Compounds on the Properties of Steel/Aluminum Laser Welded Joints*[D], Changsha: Hunan University, 2021 (in Chinese)

11 Danbi S, Ryoonhan K, Kwangdeok C *et al. Metals*[J], 2023, 13(5): 916

12 Wang L, Gao M, Zhang C *et al. Materials & Design*[J], 2016, 108: 707

13 Artem A V, Vladimir G P, Dmitriy A A *et al. Materials*[J], 2022, 15(3): 722

14 Yang J W, Liu X Y, Li Tao *et al. Journal of Iron and Steel Research International*[J], 2024, 31(10): 2463

15 Shahin S, Seyedeh F N, Reihaneh E *et al*. *Lasers in Manufacturing and Material Processing*[J], 2024, 11(3): 743

16 Li J Z, Liu Y B, Zhen Z Y *et al. Optics & Laser Technology*[J], 2021, 134: 106594

17 Wang Luoxin, Liu Cengjie, Wei Xicheng *et al. Hot Working Technology*[J], 2025, 54(11): 131 (in Chinese)

18 Li Songzhao, Zhu Jialei, Song Kuangda *et al. China Surface Engineering*[J], 2025, 38(1): 265 (in Chinese)

19 Guo N, Cheng Q, Fu Y L *et al*. *Surface and Coatings Technology*[J], 2023, 473: 129984

20 Xie J L, Zhou Y H, Zhou C P *et al*. *Journal of Materials Research and Technology*[J], 2024, 29: 3487

21 Yu K, Tan Z J, Zeng C Y *et al. Journal of Magnesium and Alloys*[J], 2025, 16: 101929

22 Chen G Y, Wang B, Mao S *et al*. *Optics & Laser Technology*[J], 2019, 115: 32

23 Xu F, Xu J Q, Yin Y Y *et al*. *Steel Research International*[J], 2023, 94(10): 2200923

24 Wang Z C, Paschalidou E M, Seyeux A *et al*. *Frontiers in Materials*[J], 2019, 6: 232

921A钢局部干法水下摆动激光焊接接头组织及性能

朱加雷，王俞轲，曾才有，李守根，朱文磊，邵明星，杨子龙

(北京石油化工学院 机械工程学院，北京 102627)

摘　要：针对舰船较深裂纹原位修复需求，对921A钢开设4 mm深30°U型坡口，采用局部干法水下摆动激光填丝焊接工艺进行了空气和浅水环境坡口填充试验，并进一步对其组织性能进行分析。结果表明：空气与浅水环境焊缝成型良好且无明显焊接缺陷，由于局部干腔保护气及水下速冷作用使得浅水焊缝表面呈现亮白色密集鱼鳞纹；空气环境焊缝针状铁素体较多，水环境的冷却作用使得浅水环境焊缝板条状马氏体较多。能谱分析结果显示，两种环境下主要合金元素在熔合线附近均呈平缓过渡，冶金结合良好；但浅水环境冷却速率更高，导致元素分布波动更大，且焊缝中Si、Mn、Mo含量更高，Cr含量略低。空气环境与浅水环境焊缝的硬度在各区域趋势较为一致，但浅水环境焊缝整体硬度高于空气环境焊缝。拉伸断裂位置均位于母材区域，焊缝拉伸强度和屈服强度顺序为：浅水环境焊缝＞空气环境焊缝＞母材。电化学腐蚀检测表明浅水环境焊缝的耐腐蚀性较差于空气环境焊缝。

关键词：摆动激光焊接；921A舰船钢；局部干法水下焊接；微观组织；力学性能

作者简介：朱加雷，男，1981年生，博士，教授，北京石油化工学院机械工程学院，北京 102627，E-mail：zhujialei@bipt.edu.cn